SOLAR CELLS

Bandgap-universal passivation enables stable perovskite solar cells with low photovoltage loss

Yen-Hung Lin[1,2,3]*, Vikram[4]†, Fengning Yang[1]†, Xue-Li Cao[2,3]†, Akash Dasgupta[1]†, Robert D. J. Oliver[1,5]†, Aleksander M. Ulatowski[1]†, Melissa M. McCarthy[1], Xinyi Shen[1], Qimu Yuan[1], M. Greyson Christoforo[1], Fion Sze Yan Yeung[2,3], Michael B. Johnston[1], Nakita K. Noel[1], Laura M. Herz[1], M. Saiful Islam[4], Henry J. Snaith[1]*

The efficiency and longevity of metal-halide perovskite solar cells are typically dictated by nonradiative defect-mediated charge recombination. In this work, we demonstrate a vapor-based amino-silane passivation that reduces photovoltage deficits to around 100 millivolts (>90% of the thermodynamic limit) in perovskite solar cells of bandgaps between 1.6 and 1.8 electron volts, which is crucial for tandem applications. A primary-, secondary-, or tertiary-amino–silane alone negatively or barely affected perovskite crystallinity and charge transport, but amino-silanes that incorporate primary and secondary amines yield up to a 60-fold increase in photoluminescence quantum yield and preserve long-range conduction. Amino-silane–treated devices retained 95% power conversion efficiency for more than 1500 hours under full-spectrum sunlight at 85°C and open-circuit conditions in ambient air with a relative humidity of 50 to 60%.

Although metal-halide perovskites are considered "defect-tolerant" (*1*, *2*), they still require careful crystallization and growth (*3*, *4*). Furthermore, defect passivation through molecular bonding (*5*) or incorporating organic cations that form low-dimensional perovskites that interface to form a passivation "heterojunction" with the three-dimensional (3D) perovskite (*6*–*8*) is required to reach the highest power conversion efficiency (PCE) and exhibit improved long-term operational stability in optoelectronic devices (*9*–*11*). For isolated perovskite thin films or nanocrystals, a broad range of approaches can be adopted, including the use of molecular Lewis acids or bases (*12*, *13*) and ligands that are typically used in nanocrystal growth, such as trioctylphosphine oxide (*14*) and oleic acid (*15*). Large organic molecules that can lead to internal luminescence efficiency approaching unity in polycrystalline perovskite films (*16*) and yield stable passivation often inhibit charge-carrier transport in perovskite films and have yet to be demonstrated in high-performance solar cells (*17*).

For more molecularly defined passivation, amine-based functional groups have emerged as a key component because of their strong binding energies to the perovskite surface (*18*–*21*). Despite demonstrating exceptional photoluminescence quantum yield (PLQY) properties in passivated perovskite films, some of these amine-based molecular passivation strategies have yet to be proven effective in achieving high efficiency or photovoltaic (PV) parameters near the radiative limit (*18*–*20*). The challenge in translating the enhanced PLQY observed in passivated perovskite films into comparable PCE gains in full solar cell devices underscores a gap in our present understanding.

This gap pertains to how amine-based and, more broadly, Lewis base–based molecules contribute to effective defect passivation (*18*–*21*). Additionally, optimizing passivation strategies for wider-bandgap perovskites, which consist of mixed halides and cations, remains crucial for the development of tandem solar cells (*22*). This need is especially pertinent because most presently used passivation strategies are predominately designed for narrow-bandgap perovskites with compositions near $FAPbI_3$ (where FA is formamidinium) (*9*, *21*, *23*, *24*), and thus, versatile strategies applicable across a broader spectrum of perovskite compositions are lacking.

In this work, we used a series of amino-silane molecules (Fig. 1A) with various types of amines (primary, secondary, tertiary, or combinations thereof) to explore the underlying optoelectronic and material mechanisms and devise a universal passivation strategy for perovskites with bandgaps ranging from 1.6 to 1.8 eV. Using the identified efficient amino-silane molecules, we demonstrate medium-area (0.25 cm^2) and large-area (1 cm^2) perovskite solar cells that exhibit PCEs derived from maximum power point tracking (MPPT) that reach 22.4 and 21.9%, 20.7 and 20.1%, and 18.6 and 18.4% for 1.60-, 1.67-, and 1.77-eV mixed-cation, mixed-anion–based perovskites, respectively.

All perovskite solar cells passivated with best-performing amino-silane molecular compound achieved photovoltage deficits as low as 100 to 120 mV, thus surpassing 90% of the maximum photovoltage dictated by thermodynamic detailed balance theory. Furthermore, our passivation strategy notably enhanced the durability of perovskite solar cells, allowing them to retain 95% efficiency for more than 1500 hours under full-spectrum simulated sunlight. Our aging was conducted without ultraviolet (UV) filters, at an elevated temperature of 85°C, and under open-circuit conditions in ambient air with a relative humidity of 50 to 60%.

Impacts of amino-silane molecules on metal-halide perovskites

We investigated the impact of primary amine–based (3-aminopropyl)trimethoxysilane (APTMS; see Fig. 1A) molecules using vapor-phase treatment on mixed-cation lead, mixed-anion perovskite thin films and their corresponding positive-intrinsic-negative (p-i-n) perovskite solar cells. We show schematics of the device architecture and the film passivation process in Fig. 1, B and C, respectively. For the perovskite light absorber, we used an "MA-free" (where MA is methylammonium) composition—$Cs_{0.13}FA_{0.87}Pb(I_{0.9}Br_{0.1})_3$, hereafter abbreviated as $Cs_{13}Br_{10}$—that had a bandgap of 1.6 eV and was suitable for the middle subcell of triple-junction perovskite tandem solar cells (*25*). We measured a substantial increase in PLQY (from ~6 to 24%) for perovskite films before and after the APTMS treatment.

For integration into p-i-n PV devices, we used [4-(3,6-dimethyl-9H-carbazol-9-yl)butyl]phosphonic acid (Me-4PACz) and [6,6]-phenyl-C61-butyric acid methyl ester ($PC_{61}BM$) as the hole-transport and electron-transport materials, respectively. For further details, see the materials and methods section of the supplementary materials for a description of the full-device fabrication protocol. The current density–voltage (*J-V*) characteristics and other corresponding PV performance parameters obtained from our APTMS-treated and reference solar cells are shown in fig. S1. Despite the boost in PLQY of the isolated perovskite films, the PV performance of APTMS-treated cells was much worse than our reference cells, and exhibited substantial hysteresis in the *J-V* characteristics. This unexpected outcome led us to delve deeper into the effects of passivation using amino-silane molecules.

Silane molecules are used to treat silicon wafers to alter their surface properties (*26*), where Si-O-Si bonds are formed, and the additional moieties alter the surface energy of the wafer. The treatments do not necessarily lead to a single molecular monolayer, and thicker cross-linked films of (hydrated) silicon oxide can form. When treating the perovskite films with amino-silane molecules, such as APTMS,

[1]Department of Physics, University of Oxford, Clarendon Laboratory, Parks Road, Oxford OX1 3PU, UK. [2]Department of Electronic and Computer Engineering, The Hong Kong University of Science and Technology, Clear Water Bay, Kowloon, Hong Kong SAR. [3]State Key Laboratory of Advanced Displays and Optoelectronics Technologies, The Hong Kong University of Science and Technology, Clear Water Bay, Kowloon, Hong Kong SAR. [4]Department of Materials, University of Oxford, Parks Road, Oxford OX1 3PH, UK. [5]Department of Materials Science and Engineering, University of Sheffield, Mappin Street, Sheffield S1 3JD, UK.
*Corresponding author. Email: yh.lin@ust.hk (Y.-H.L.); henry.snaith@physics.ox.ac.uk (H.J.S.)
†These authors contributed equally to this work.

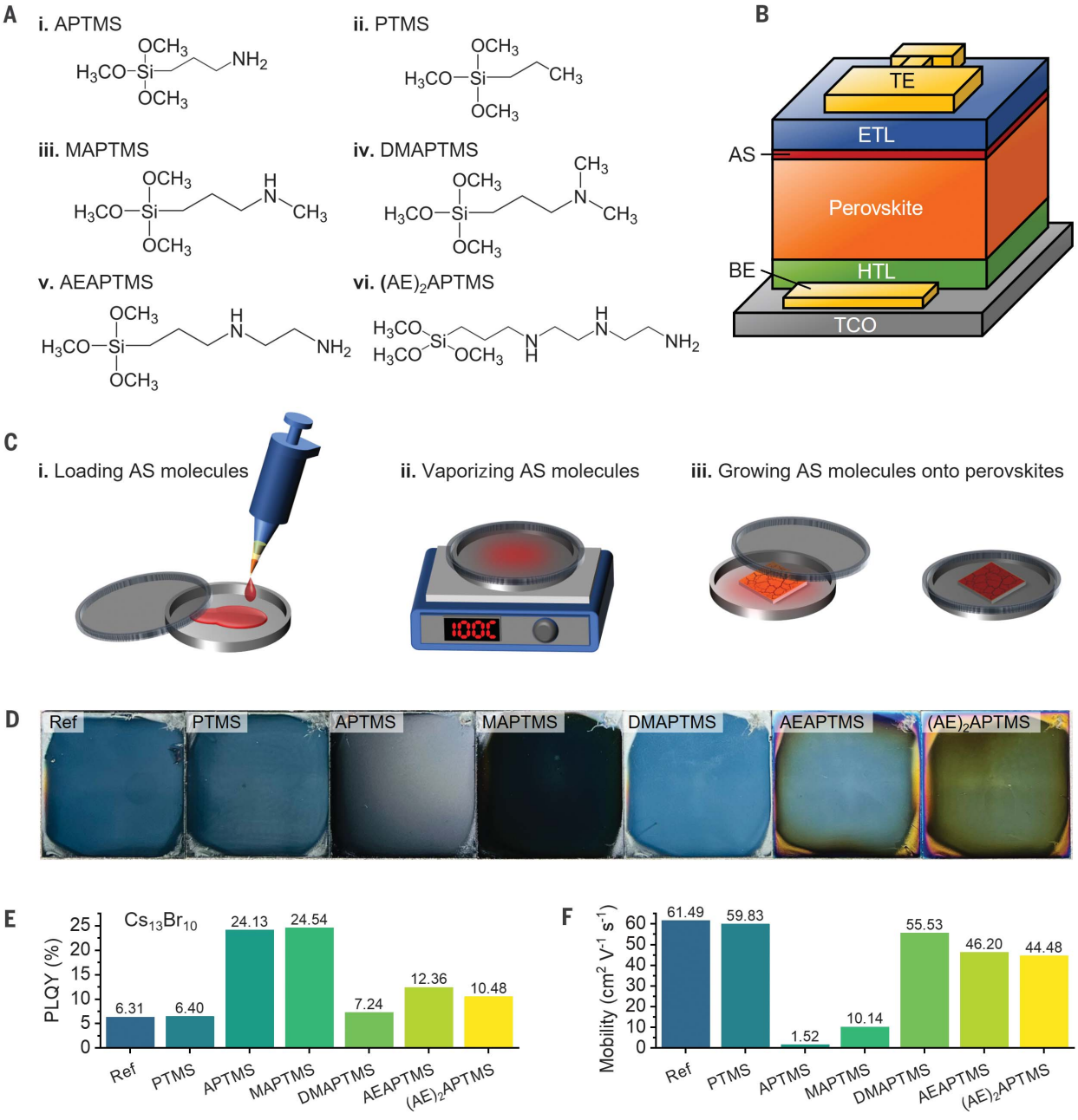

Fig. 1. Amino-silane molecules and their fabrication and optoelectronic properties. (**A**) Structures of the amino-silane molecules APTMS, PTMS, MAPTMS, DMAPTMS, AEAPTMS, and $(AE)_2$APTMS. (**B**) Schematic of a p-i-n solar cell architecture. AS, amino-silane; BE, bottom electrode; TCO transparent conductive oxide; TE, top electrode. (**C**) Illustration of the vapor-based deposition adopted for passivation molecules: (i) loading an amino-silane molecule chosen from Fig. 1A n a petri dish, (ii) heating the petri dish that contains the passivation molecule at 100°C for a few minutes until all the molecules are vaporized, and (iii) placing an as-grown perovskite film sample inside the petri dish for tens of seconds to a couple of minutes (see fig. S5 for the optimal AEAPTMS exposure time). (**D**) Photos of perovskite films made on ITO glass substrates and treated with the molecules shown in Fig. 1A and without any treatment (Ref, reference). (**E** and **F**) PLQY (E) and THz mobility (F) of $Cs_{13}Br_{10}$ perovskite films treated with the molecules shown in Fig. 1A and without any treatments (Ref).

both the silane units and the amine units may interact with the perovskite surface and each other, hence influencing their growth (*18*, *19*).

To understand how the structure of amino-silane molecules affects perovskites, apart from APTMS, we treated perovskite thin films with amino-silane molecules with various types of amines, and silane molecules alone. These molecules include secondary amine–based trimethoxy[3-(methylamino)propyl]silane (MAPTMS), tertiary amine–based (*N*,*N*-dimethylaminopropyl)trimethoxysilane (DMAPTMS), and primary and secondary amine–based [3-(2-aminoethylamino)propyl]trimethoxysilane (AEAPTMS) and 3-[2-(2-aminoethylamino) ethylamino]propyltrimethoxysilane [$(AE)_2$APTMS], as well as the alkyl-silane molecule trimethoxy(propyl)silane (PTMS), which is absent of amine moieties. The corresponding molecular structures are drawn in Fig. 1A. In Fig. 1D, we show photographs of perovskite films treated with

these (amino-)silane molecules and a reference film without any treatment.

We examined perovskite thin films with the compositions of $Cs_{13}Br_{10}$ and $Cs_{0.15}FA_{0.85}Pb(I_{0.6}Br_{0.4})_3$, hereafter abbreviated as $Cs_{15}Br_{40}$. The latter had a PV bandgap of 1.77 eV (*27*) and is widely used as the top cell in perovskite/perovskite tandem solar cells (*28*–*30*). Except for PTMS, all of the amino-silane molecules improved the PLQY for $Cs_{13}Br_{10}$ as compared to the reference (as shown in Fig. 1E), whereas for $Cs_{15}Br_{40}$, the PLQY was improved after treatment with all of the molecules apart from PTMS and DMAPTMS (fig. S2). In particular, for the wider-bandgap $Cs_{15}Br_{40}$ perovskite, we only observed an increase in PLQY from ~1.5 to 3% for the APTMS treatment. However, this value increased to >7% and to >20% for the AEAPTMS and $(AE)_2$APTMS treatments, respectively.

We then conducted a series of PLQY measurements under 1-sun-equivalent photoexcitation on a variety of perovskite films and "half-stacks." These were composed of either indium tin oxide (ITO) glass/hole transport layer (HTL, Me-4PACz with a wetting layer formed of aluminum oxide nanoparticles)/perovskite or glass/aluminum oxide nanoparticles/perovskite/electron transport layer [ETL, containing $PC_{61}BM$ with a hole blocking layer formed of bathocuproine (BCP)] using AEAPTMS (figs. S3 to S5). We observed the most pronounced improvement in PLQY from the amino-silane molecules that contained both primary and secondary amine groups [i.e., AEAPTMS and $(AE)_2$APTMS; Fig. 1E].

Because PLQY is indicative of a solar cell's behavior at the open-circuit condition, maximized photoluminescence (PL) in these half-stacks is crucial for achieving higher photovoltages due to reducing nonradiative recombination losses. For example, perovskite/ETL films treated with AEAPTMS molecules, including $Cs_{13}Br_{10}$, $Cs_{15}Br_{40}$ and $Cs_{0.17}FA_{0.83}Pb(I_{0.77}Br_{0.23})_3$, hereafter abbreviated as $Cs_{17}Br_{23}$, had a notable 60-fold increase in PLQY (see fig. S4A), with the PLQY for the glass substrate/$Cs_{15}Br_{40}$/ETL stack increasing from 0.07% for the control to 4.1% for the AEAPTMS-treated films. In fig. S4B, we also show their corresponding calculated quasi-Fermi level splitting (QFLS) values for further comparison (*31*). Thus, the AEAPTMS passivation specifically inhibited nonradiative recombination at the perovskite/ETL interface, which is generally regarded as the most lossy part in a p-i-n perovskite solar cell (*27*, *32*).

Because we observed the largest enhancement in the PLQY for the perovskite composition of $Cs_{13}Br_{10}$ when using APTMS, we performed UV-visible (UV-vis) absorption spectroscopy and noncontact transient terahertz (THz) photoconductivity measurements on $Cs_{13}Br_{10}$ films to probe the impact of the amino-silane passivation further. In fig. S6, we show UV-vis absorption spectra of $Cs_{13}Br_{10}$ perovskite films with and without passivation. For the perovskite film passivated with APTMS, we observed a considerable reduction in the optical density, less than half over the entire absorption range, which indicates a bulk change to the perovskite film after passivation rather than just at the surface. All the other passivated films exhibited a small reduction in optical absorption in comparison with the reference film.

Optical pump THz probe spectroscopy reveals the change in conductivity of a sample after photoexcitation and can be used to determine the "short-range" charge-carrier mobility (see supplementary text). This technique revealed surprising differences between our perovskite films (Fig. 1F and figs. S7 and S8). For the reference films, the sum of electron and hole mobilities was ~60 $cm^2 V^{-1} s^{-1}$, which is a high value for lead-halide perovskites (*33*). For all the passivation treatments, apart from PTMS, the mobilities were reduced (Fig. 1F). For the APTMS-treated $Cs_{13}Br_{10}$ film, this reduction in mobility was precipitous, with values dropping to 1.5 $cm^2 V^{-1} s^{-1}$. This drop in mobility indicates a major disruption to the crystalline order throughout the APTMS-treated perovskite films on a length scale short enough to inhibit the THz-derived charge-carrier mobility. By contrast, the reduction in charge-carrier mobility was much less severe for the other passivation molecules that we investigated; for example, we determined a sum mobility of 46 $cm^2 V^{-1} s^{-1}$ for the AEAPTMS-treated films.

With such a severe disruption to crystalline order for the APTMS-treated films, which was inferred from both the drop in THz mobility and the optical absorption strength, we tried to discern changes in the morphology or crystallinity of the thin films by electron microscopy and x-ray diffraction (XRD). We first investigated the influence of different amino-silane molecules on the film formation quality by examining the surface morphology of the $Cs_{13}Br_{10}$ perovskite films by scanning electron microscopy (SEM; fig. S9). We observed the characteristic polycrystalline morphology in all the perovskite films, with apparent grain sizes in the range of 150 to 200 nm. However, SEM images are a very coarse indication of grain size, and there are many examples of metal-halide perovskites where the crystalline domain size, as studied by high-resolution electron microscopy, is much smaller than the apparent size in SEM images (*34*, *35*). The apparent grains observed in SEM images of the APTMS-treated perovskite film, although resembling those in the reference in size, could equally represent interaggregate grains of much smaller sizes rather than genuine grains of single-crystalline domains. In addition to the apparent remaining grains, for both the APTMS- and MAPTMS-treated perovskite films, more than 50% of the film surfaces appeared to be ill-defined and "cloudy." This effect could be caused by a complete change to the morphology within these regions or the presence of a thick "capping layer" of an amorphous material. For the AEAPTMS- and $(AE)_2$ APTMS-treated films, the polycrystalline structures were discernible over the entire surface area, but there is more "haziness" to the images, which is suggestive of a surface coating with an insulating material.

In fig. S10, we show XRD 2θ plots for the series of treated films, which again reveal notable differences. The XRD traces of PTMS-, DMAPTMS-, and AEAPTMS-treated $Cs_{13}Br_{10}$ films did not differ appreciably from those of the untreated reference films, and all exhibited the characteristic XRD pattern of polycrystalline perovskite films without any additional diffraction peaks or changes in scattering intensities (*36*). For the $(AE)_2$APTMS-treated perovskite film, we observed a slight decrease in peak intensities, with the full width at half maximum (FWHM) of the perovskite peaks broadening. Meanwhile, the corresponding peaks for the AEAPTMS-treated film showed narrowing FWHM values compared with those of the untreated perovskite film (see supplementary text and table S1). However, for the APTMS-treated $Cs_{13}Br_{10}$ film, all the scattering peaks were reduced in intensity by more than an order of magnitude.

Taken together, the THz mobility measurements, XRD patterns, and UV-vis absorption spectra indicate that the APTMS molecules strongly influenced the crystallinity throughout the perovskite films, introducing short-range scattering defects or disrupting the crystalline domains to such an extent that the charge carriers underwent short-range scattering and had severely limited charge-carrier mobility. However, for previous measurements of perovskite nanocrystals with a crystal diameter of 10 nm, the charge-carrier mobility is only reduced by a factor of three, versus the bulk mobility in a polycrystalline $CsPbBr_3$ film (*33*, *37*). Here, the reduction in mobility by a factor of 40 indicated that the complete breakup of the crystalline order, or introduction of charge-scattering sites, occurred on a much shorter length scale than 10 nm. By contrast, applying AEAPTMS and $(AE)_2$APTMS molecules appeared to leave the crystalline order and charge-carrier mobility largely unaffected but still enable an equally substantial increase in PLQY.

Insights of passivation molecule formation and surface bonding interactions

Despite these results, it remained unclear why different types of amines, whether primary (such as APTMS) or secondary (such as MAPTMS), could have vastly different impacts on perovskite films. To explore how APTMS, MAPTMS, and AEAPTMS affected metal-halide perovskites in more detail, we used grazing-incidence

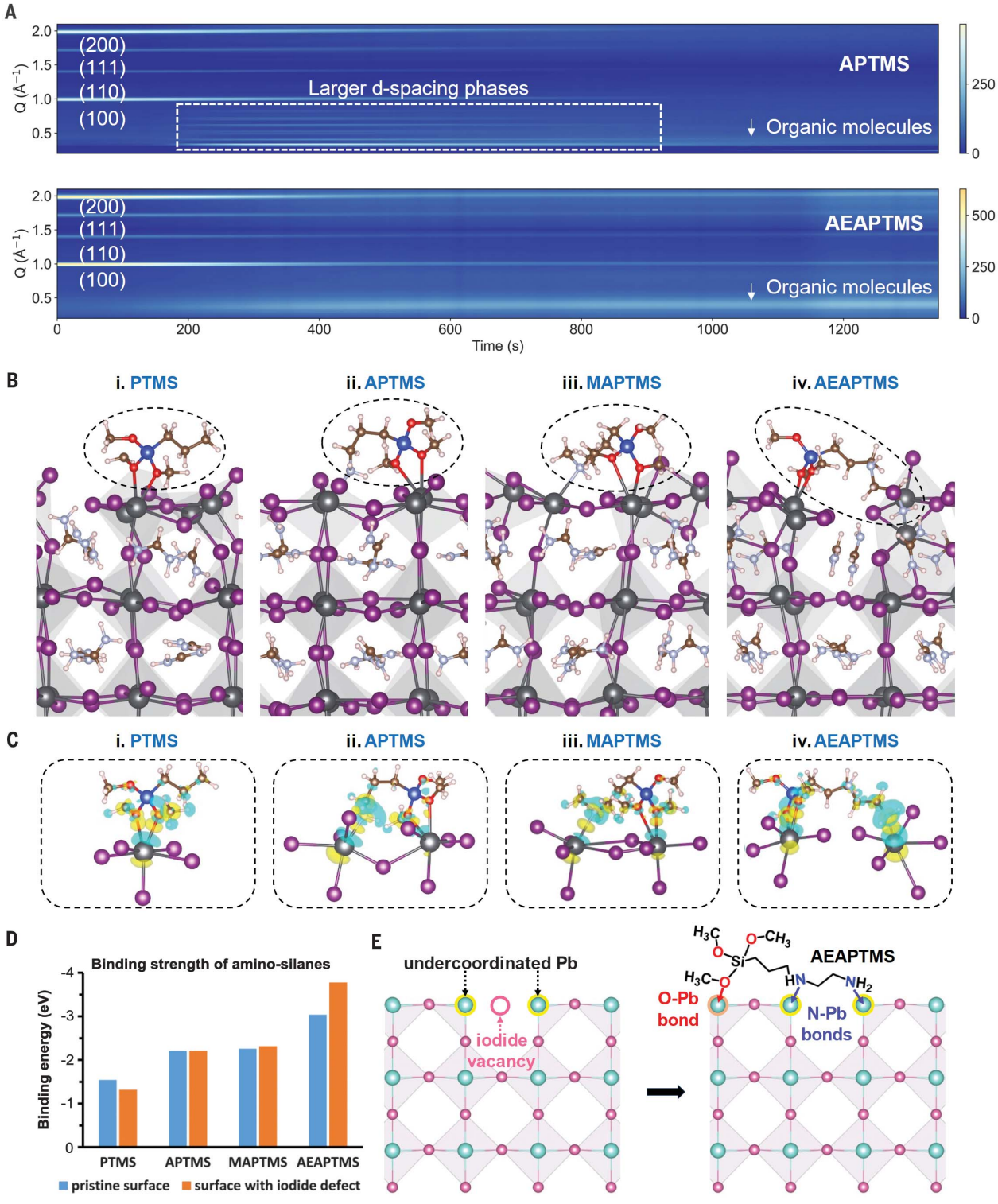

Fig. 2. Structural analysis of the amino-silane surface interactions. (**A**) Time-dependent GIWAXS patterns measured at incident angles of 1° for the vapor-based treatment with APTMS (top) and AEAPTMS (bottom) on $I_{0.9}Br_{0.1}$ perovskite films, with the background signals from air scattering, Kapton-taped window, glass, and ITO removed. The slight tilt observed in all the signals acquired with time was caused by the thermal extension of the sample stage, which caused a partial loss of alignment. (**B**) Side views of the simulated structures using DFT and AIMD techniques of the interactions of the amino-silanes PTMS, APTMS, MAPTMS, and AEAPTMS (identified by the dashed ovals) with the Pb/I terminated (001) $FAPbI_3$ surface. PbI_6 octahedra are highlighted to show that the major structural relaxation is found mostly in the uppermost layer. (**C**) Changes in the charge-density profile around all the species involved in the silane-surface binding; the prominent charge accumulation (yellow) and depletion (blue) regions show N-Pb and O-Pb interactions. (**D**) Binding energies of amino-silanes on the pristine surface (blue) and on the iodide vacancy defect surface (orange). (**E**) Schematic diagram showing the perovskite surface with undercoordinated Pb cations adjacent to an iodide vacancy and the binding of an AEAPTMS molecule through N-Pb and O-Pb bonds. Here, FA^+ cations are omitted for clarity.

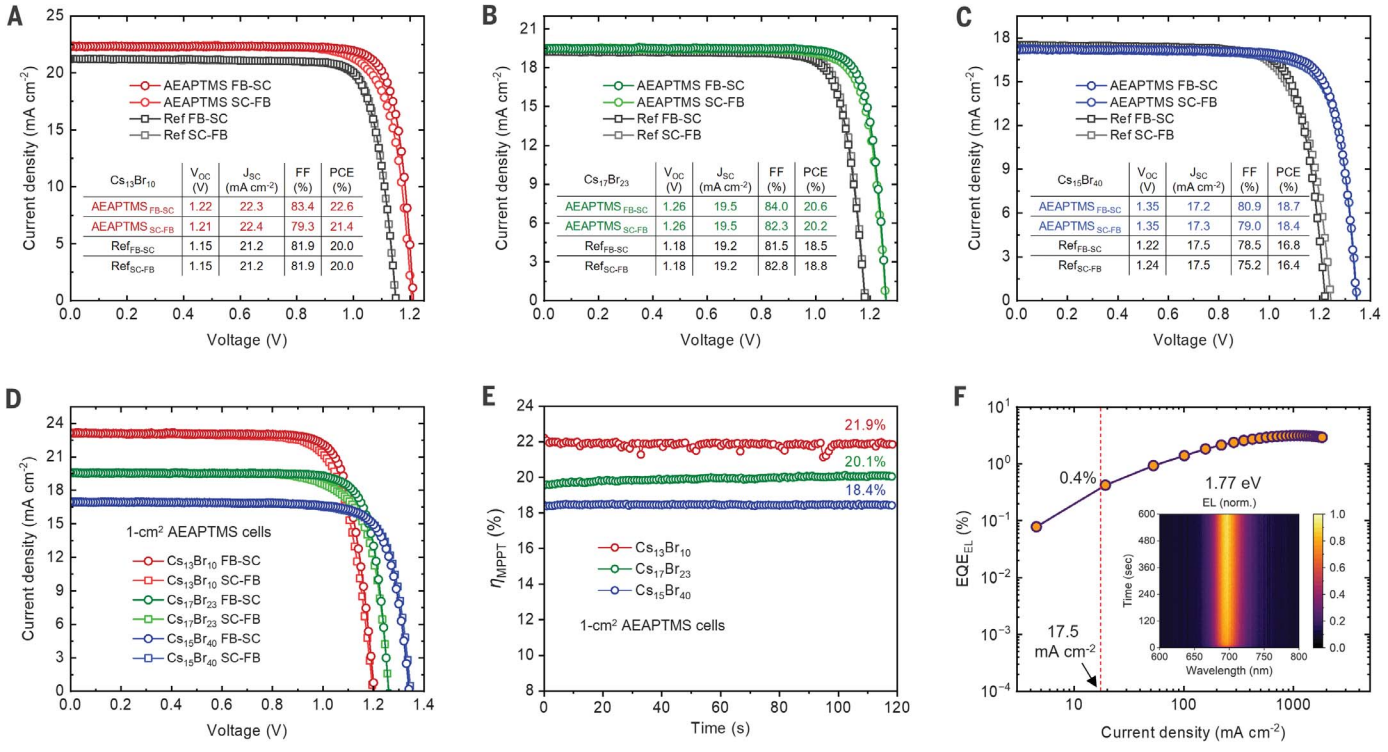

Fig. 3. Perovskite solar cell characterization. (**A** to **C**) Current density and voltage characteristics of the representative AEAPTMS-treated perovskite solar cells with an aperture size of 0.25 cm^2 using an absorber composition of $Cs_{13}Br_{10}$ (A), $Cs_{17}Br_{23}$ (B), or $Cs_{15}Br_{40}$ (C), where FB-SC indicates the scan direction from the FB to SC condition, and vice versa for SC-FB. Insets of (A) to (C) summarize critical PV performance parameters. (**D** and **E**) Current density and voltage characteristics of the representative large-area 1-cm^2 AEAPTMS-treated cells based on the compositions of $Cs_{13}Br_{10}$, $Cs_{17}Br_{23}$, and $Cs_{15}Br_{40}$ are shown in (D), and the corresponding MPPT efficiencies (η) for 120 s are shown in (E). (**F**) EQE_{EL} as a function of injection current densities, where the current density of 17.5 mA cm^{-2} results in an EQE_{EL} of 0.4%. The EQE_{EL} data were obtained under the operation of a voltage sweep between 0 and 4 V (fig. S30C) for an AEAPTMS-treated $Cs_{15}Br_{40}$-based perovskite solar cell (fig. S30, A and B). The inset shows the normalized electroluminescence (EL) spectrum under a current injection of 17 mA cm^{-2} over the course of 600 s, whereas the EQE_{EL} data tracked over 600 s are shown in fig. S30D.

wide-angle x-ray scattering (GIWAXS) to study their effects on the orientation and crystallinity of treated $Cs_{13}Br_{10}$ perovskite films. First, we used an ex situ GIWAXS setup to survey as-treated perovskite thin films (figs. S11 and S12). We initially used GIWAXS at a lower incidence angle (0.5°), which provides information about the surface region with an attenuation length of ~70 nm (see supplementary text). For the APTMS-treated perovskite films, there were no clear Debye-Scherrer diffraction rings observed in the GIWAXS patterns (fig. S11), consistent with the 2θ XRD scans. By contrast, for the AEAPTMS-treated perovskite films, we observed a higher scattering intensity in the small-angle GIWAXS scans than in the untreated films.

At the higher incidence angle (1.5°), we obtained information about the deeper regions within the perovskite films. We observed continuous Debye-Scherrer diffraction rings, but with differing intensities, at scattering wave vector Q_{xy} of 1.0, 1.4, 1.7, or 2.0 Å^{-1} in all of the APTMS-, AEAPTMS-, and MAPTMS-treated films (fig. S11), which, respectively, corresponded to (100), (110), (111), and (200) diffraction peaks in 1D XRD patterns (fig. S10). For the MAPTMS-treated perovskite films, a series of discrete scattering points in the low-Q space were observed that we assigned to a highly oriented 2D species (figs. S11 and S12). The relative intensities of these peaks, compared with that of the main perovskite peaks, were higher in the low-angle GIWAXS scans, indicating that the material responsible was predominantly located near the top of the perovskite films. We further elaborate on these observations, including their orientation and layer spacing, in the supplementary text and fig. S13.

Next, we used a synchrotron-based in situ GIWAXS setup (see fig. S14) to gain insight into the evolution of perovskite film crystallinity during the vapor-based amino-silane treatment. For these measurements, our treatment conditions were adapted to be compatible with the synchrotron environment, so the treatment times were considerably extended. The in situ time-dependent GIWAXS patterns are shown in Fig. 2A for the APTMS- and AEAPTMS-treated films, and the pattern evolutions were recorded in movies S1 to S4.

The time-dependent GIWAXS patterns of the APTMS-treated perovskite films were highly revealing (Fig. 2A and movies S1 and S2). Between 150 and 450 s, a highly intense series of low-Q reflection rings appeared, indicating the emergence of larger d-spacing scattering features, which could, for example, be a lower-dimensional perovskite phase. At ~600 s, the newly emerged low-Q scattering rings and the main perovskite scattering rings rapidly faded until they became indiscernible after ~1000 s. These results were consistent with the APTMS molecules first causing a structural transformation followed by "disintegration" of the perovskite structure.

Coupled with the knowledge that primary amines can strongly interact with and "solvate" metal-halide perovskites (*38*, *39*), our observations indicated that the perovskite films underwent a solvation process during the APTMS treatment by reacting with primary amines, crystallizing into an intermediate species with a larger d-spacing than the ABX_3 perovskites, as seen in Fig. 2A, and then completely breaking down and losing nearly all of their crystallinity. This APTMS-triggered solvation process resulted in a noticeable visual transformation of the treated films that caused them to become

"hazier" and more transparent (see movie S5). The peculiarity is that the UV-vis absorption spectra indicated that at least half of the absorption strength remained, and the PLQY remained extremely strong (Fig. 1E), with a small blueshift in the emission peak as compared with that of the reference perovskite films (fig. S15). These findings imply that the 3D perovskite structure, although undergoing substantial transformation, partially remained present in a modified but well-passivated form, corroborating our observation that exposure to APTMS molecules gradually solvate the 3D perovskite phase (Fig. 2A).

For the AEAPTMS-treated perovskite films, the evolution in GIWAXS patterns was less pronounced (Fig. 2A and movies S3 and S4). The relative intensity ratio of perovskite rings remained consistent throughout the entire AEAPTMS treatment, and there was no evidence of an emergence of discrete larger d-spacing phases. This result indicated that the isotropic orientation of the bulk perovskite was maintained before and after the AEAPTMS treatment. The absolute intensities of all the perovskite peaks did become weaker with time, and a pair of broad, amorphous rings appeared in the low *Q*-space, which we interpreted to belong to the organic molecules of AEAPTMS. This result indicates that during this in situ treatment, AEAPTMS molecules coated and accumulated onto the surface of the perovskite film with a long processing time (~30 min; movies S3 and S4), which might have screened the x-ray scattering from the underlying perovskite film.

To verify whether the different passivation treatments were located on the film surface or were penetrating throughout the bulk of the films, we further examined the films using time-of-flight secondary ion mass spectrometry (TOF-SIMS), looking at the elemental depth profile. Although APTMS (fig. S16A) and MAPTMS (fig. S16B) both exhibited varying degrees of Si-signal penetration throughout the films. The Si signal for perovskite films treated with AEAPTMS molecules remained predominantly within the surface region of the perovskite layer (fig. S16C). This observation held even when the treatment duration was tripled (fig. S16D).

The structures and interactions of the amino-silane molecules at perovskite surfaces were, however, not fully understood at the atomic level. To gain further insights into such properties, we used density functional theory (DFT) and ab initio molecular dynamics (AIMD) methods to investigate four types of silane molecules covering different possible amine positions—primary (APTMS), secondary (MAPTMS), and both primary and secondary (AEAPTMS)—as well as in the absence of an amino group (PTMS) (see supplementary text). Their interactions on the pristine perovskite surface and on surfaces with an iodide vacancy defect were examined. Iodide vacancy defects play highly detrimental roles in affecting the operational efficiency and stability of perovskite solar cells, including facilitating ion migration to surfaces (*40*–*42*) and nonradiative photocarrier recombination (*43*, *44*). To investigate key adsorption and structural trends for the range of amino-silanes on FA-based, MA-free perovskite triiodides, we examined the (001) PbI_2 terminated pristine $FAPbI_3$ surface because it is one of the most stable and studied halide perovskite surfaces (*45*, *46*). We provide computational details in the supplementary materials.

Figure 2, B and C, shows the optimized structures and calculated binding energies of the amino-silane molecules (Fig. 2D) on the pristine surface and on the iodide vacancy defect surface. Three important features emerged. First, favorable binding energies showed strong bonding affinity between the molecules and the surface, with the highest and lowest binding energies found for AEAPTMS and PTMS, respectively; however, only for AEAPTMS did the surface binding energy increase substantially from the pristine surface to the iodide vacancy defect surface. Second, the strongest adsorption for AEAPTMS suggested the role of larger amino-silane molecules that have both primary and secondary amine groups in providing effective surface defect passivation. As surface Pb ions adjacent to an iodide vacancy were severely undercoordinated (with fourfold coordination versus octahedral in the bulk of perovskites), the strong passivator adsorption of AEAPTMS increased the coordination around these Pb ions and eliminated the effects of surface vacancy defects (Fig. 2E and fig. S17). Third, noting the speculation around the precise atomistic interactions of the amino-silane molecules at the perovskite surfaces (*18*), our simulations revealed that the terminal amines in AEAPTMS bind to the surface Pb atoms with an N-Pb bond length of 2.51 Å, versus the longer Pb-I bond length of 3.15 Å. The schematic in Fig. 2E shows that the AEAPTMS molecule bridged the two Pb ions adjacent to the iodide vacancy through N-Pb bonds.

In addition to speculation around N-Pb interactions from previous work (*18*), we also observed O-Pb bonding with an average bond length of 2.80 Å. Changes in the charge-density profile around all the species (Fig. 2C) showed silane-surface charge transfer around the surface Pb cations, again indicating O-Pb and N-Pb chemical bonds. Such multidentate interactions increased the binding or anchoring strength on the surface and enhanced the effective passivation. Overall, these ab initio simulation results also agreed with our experimental findings and provide new structural and mechanistic insights at the atomic level.

PV cell operational performance and stability

We fabricated and measured a series of solar cells (fig. S18; the designs of our cell layouts are shown in fig. S19) to screen all the amino-silane molecules of interest (Fig. 1A). The amino-silane molecule AEAPTMS appeared to result in the largest improvement in PV performance parameters for the $Cs_{13}Br_{10}$-based perovskite. Cells treated with $(AE)_2$APTMS also exhibited enhanced PV performance, but in many cases, we found that $(AE)_2$APTMS-treated cells showed lower short-circuit current density (J_{SC}) and fill factor (FF), and hence a lower PCE, as compared with AEAPTMS-treated cells and required a very narrow processing window, that is, <10 s, for the vapor treatment process (Fig. 1C).

We next focused on the AEAPTMS treatment. To illustrate its influence, we present representative *J*-*V* characteristics of reference and AEAPTMS-treated cells using $Cs_{13}Br_{10}$, $Cs_{17}Br_{23}$, and $Cs_{15}Br_{40}$ in Fig. 3, A to C, respectively. These cells, with an optically masked aperture of 0.25 cm^2, exhibited the corresponding PV parameters of open-circuit voltage (V_{OC}) = 1.22, 1.26, and 1.35 V; J_{SC} = 22.3, 19.5, and 17.2 mA cm^{-2}; FF = 83.4, 84.0, and 80.9%; and PCE = 22.6, 20.6, and 18.7%, respectively, for the scanning direction from forward bias to short circuit (FB-SC) conditions. Figures S20 to S22 show the corresponding external quantum efficiency (EQE) and 120-s MPPT with MPP efficiency of 22.4, 20.7, and 18.6% for $Cs_{13}Br_{10}$-, $Cs_{17}Br_{23}$-, and $Cs_{15}Br_{40}$-based cells, respectively.

The EQE analysis revealed that the integrated J_{SC} exhibited a negligible variation (<1%) compared with the J_{SC} measured from the corresponding cells under simulated sunlight, as shown in the insets of Fig. 3, A to C. The EQE-derived PV bandgaps (*31*) are 1.60, 1.67, and 1.77 eV for $Cs_{13}Br_{10}$, $Cs_{17}Br_{23}$, and $Cs_{15}Br_{40}$, respectively, with the statistical results for V_{OC}, J_{SC}, FF, and PCE shown in figs. S23 to S26, respectively. Of particular note is that V_{OC} could reach as high as 1.28 and 1.38 V for perovskites with wide bandgaps of 1.67 and 1.77 eV (i.e., $Cs_{17}Br_{23}$ and $Cs_{15}Br_{40}$), respectively. Such high photovoltages from mixed-cation, mixed-anion perovskite cells are crucial for the development of next-generation perovskite-based tandem PV cells. Because multijunction perovskite-on-silicon and all-perovskite tandem cells usually use thermally evaporated C_{60} as an ETL, to demonstrate the compatibility of our passivation treatment, we fabricated $Cs_{17}Br_{23}$ with an evaporated C_{60} and BCP ETL stack and obtained an enhancement of V_{OC} from 1.21 V for the $Cs_{17}Br_{23}$ reference cell to 1.26 V for the AEAPTMS-treated $Cs_{17}Br_{23}$ cells. This result confirmed the suitability of our approach for use in tandem cells (fig. S27).

We then proceeded to fabricate 1-cm^2 cells, and the corresponding *J*-*V* characteristics, MPPT, and EQE are shown in Fig. 3, D and E, and fig. S28, respectively. The enhancement obtained in the PV parameters for these 1-cm^2 cells (table S2) was similar to that observed in 0.25-cm^2 small-area cells with a minimum performance deficit when enlarging the cell area. Our 1-cm^2

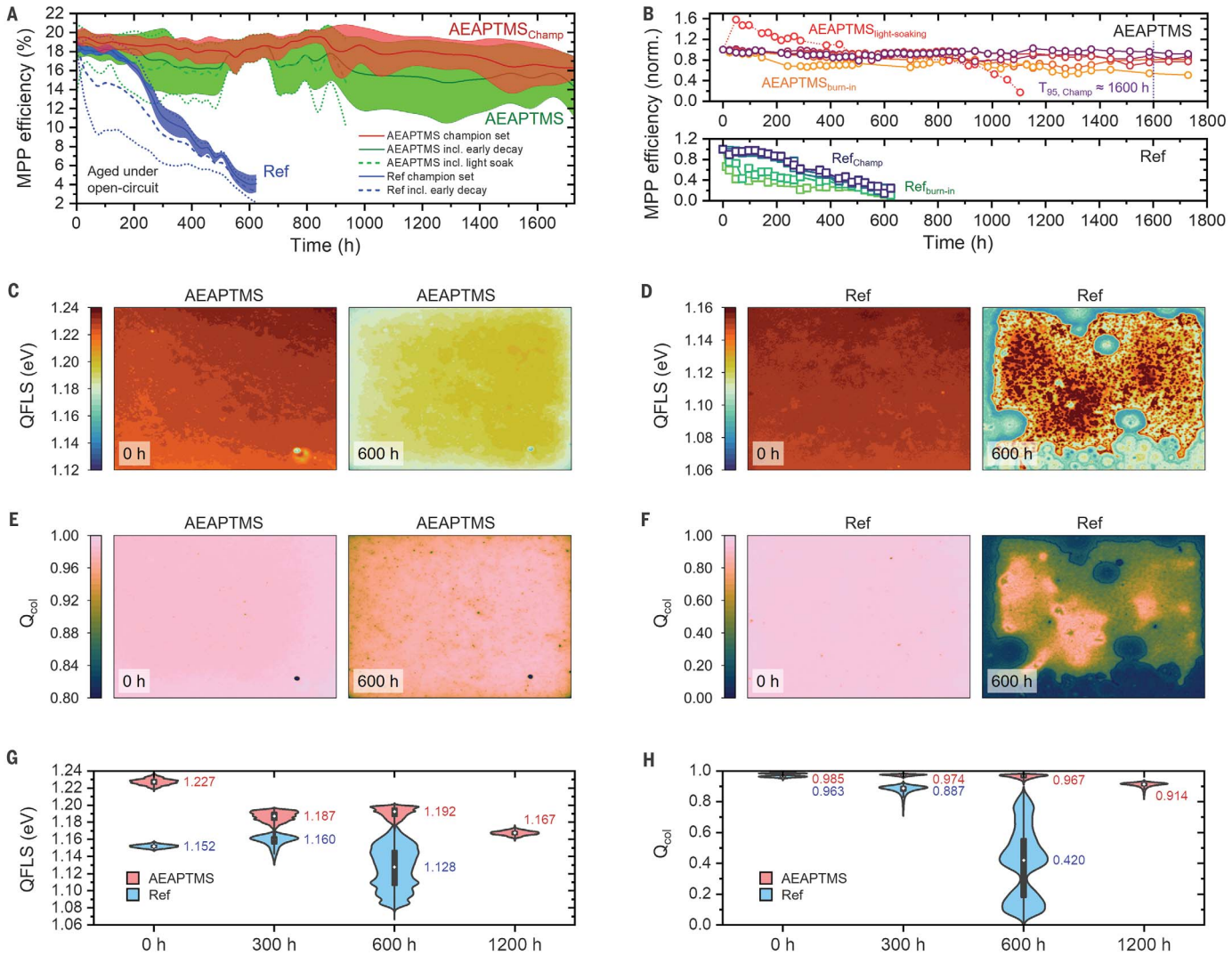

Fig. 4. Operational stability and aging characterization. (**A**) Evolution of mean MPP efficiency (with the corresponding standard deviations in a band plot) of encapsulated AEAPTMS-treated and reference (Ref) $Cs_{13}Br_{10}$ cells (including six AEAPTMS-based and five reference cells) aged under an open-circuit condition and full-spectrum 76–mW cm^{-2} simulated sunlight at 85°C (as measured and set with a black standard thermometer) in ambient air with a relative humidity in the laboratory of 50 to 60%. MPP was tracked for 120 s for each cell at different aging stages. The datasets, including some solar cells with distinct degradation pathways, that is, light soaking and burn-in, are explicitly indicated. (**B**) Evolution of normalized MPP efficiency for individual cells used and recorded for (A). For the champion cell, $T_{95,Champ}$ is approximately 1600 hours. (**C** and **D**) PL-derived QFLS maps of the full-area 0.25-cm^2 AEAPTMS-treated (C) and reference $Cs_{13}Br_{10}$ (D) cells before aging (0 hours) and after aging under the conditions described in (A) for 600 hours. (**E** and **F**) Q_{col} maps for AEAPTMS-treated (E) and reference (F) cells calculated with respect to (C) and (D), respectively. (**G** and **H**) Statistical results of QFLS (G) and Q_{col} (H) shown in a violin plot, where the median, interquartile range, and 1.5× interquartile range are indicated as a dot, a box, and a line, respectively, for all the cells recorded in (B). Each QFLS and Q_{col} map represents an area of 5.38 mm by 4.67 mm.

cell device data suggested that this vapor-based passivation approach could result in a highly uniform passivation effect. Furthermore, we estimated the thermodynamic detailed balance V_{OC} limits for the perovskite absorbers of different bandgaps and compared them with the values we obtained from our devices and the literature (fig. S29). The AEAPTMS molecule could universally boost V_{OC} to >90% of the thermodynamic limit (*31*) and resulted in outstanding performance when adopting PV cell sizes of a medium area of 0.25 cm^2 and a large area of 1 cm^2. Therefore, the photovoltages obtained from perovskite PV cells treated with AEAPTMS are approaching what has previously only been attainable from those made of single-crystal epitaxially grown III-V semiconductors (fig. S29) (*31*).

Building on this success, we further explored whether AEAPTMS could bring any additional benefits, such as inhibiting halide segregation, which often occurs in wide-bandgap mixed-halide perovskites during operation. We used a 1-cm^2 $Cs_{15}Br_{40}$-based solar cell (fig. S30, A and B) and applied a voltage sweep from 0 to 4 V to the cell while measuring the electroluminescence (Fig. 3F, fig. S30C, and movie S6). We obtained a peak electroluminescence quantum efficiency (EQE_{EL}) of 3.2% at an injection current density of ~820 mA cm^{-2} (Fig. 3F), which corresponded to exposure to illumination at an intensity of ~40 suns (based on the detailed balance limit derived 1-sun J_{SC}, which is ~20.5 mA cm^{-2}) and led to a QFLS of ~1.49 eV for a solar cell with a 1.77-eV bandgap under these high injection conditions. An EQE_{EL} of 3.2% under 1-sun irradiance would lead to a QFLS of ~1.40 eV (*31*). However, under a forward-bias injection current density near 1-sun J_{SC} (~17.5 mA cm^{-2}), we determined an EQE_{EL} of ~0.4%, which corresponded to a QFLS of ~1.35 eV. This value is in close agreement with the V_{OC}

obtained for AEAPTMS-treated $Cs_{15}Br_{40}$-based cells (fig. S23). Very encouragingly, the output spectrum of our cell could remain constant in both intensity and wavelength for 10 min at a charge-injection current density of 17 mA cm^{-2} (as shown in the inset of Fig. 3F and fig. S30D). This result matches the bandgap stability and surpasses the absolute irradiance stability of a reported state-of-the-art perovskite red-light emitting diode, which used well-passivated perovskite nanocrystals (*15*).

Next, we investigated how AEAPTMS affected a solar cell's long-term operational stability. We aged encapsulated reference and AEAPTMS-treated $Cs_{13}Br_{10}$ solar cells by exposing them to full-spectrum simulated sunlight in a xenon lamp aging box at 85°C under an open-circuit condition in ambient air with a relative humidity in the laboratory of 50 to 60%, which resembles an aging condition close to the International Summit on Organic Photovoltaic Stability ISOS-L-3 protocol (*21*, *47*, *48*). The devices were periodically taken out of the aging chamber, allowed to cool to room temperature, and characterized under 1-sun simulated sunlight at various time intervals.

The mean MPP tracked efficiency, conducted "ex situ" at specified aging times, as described above, and *J-V*–derived PCE of the aged cells, along with their standard deviations, are plotted in Fig. 4A and fig. S31A, respectively. The evolution of the corresponding PV performance parameters—V_{OC}, J_{SC}, and FF—are shown in figs. S32 to S34, respectively, and the evolutions of the MPP efficiency and PCE of each individual cell recorded are plotted in Fig. 4B and fig. S31B, respectively. Representative *J-V* curves, captured at various aging times, are presented in fig. S35. Our AEAPTMS-treated cells demonstrated substantial operational stability during the aging process. The MPP efficiency and PCE of the champion cell decreased to 95% of their initial values (i.e., $T_{95,Champ}$) after ~1600 and 1440 hours, respectively. At $T_{95,Champ}$, the MPP efficiency was recorded at 19.4% (Fig. 4B), and the PCE was 20.1% (fig. S31B). These performance metrics indicate exceptional stability for perovskite solar cells (*21*, *48*).

If we assume a linear degradation model (*47*), our stability results represent an order-of-magnitude enhancement in longevity compared with our previously reported best stability under identical aging conditions, where we reported a champion T_{80} lifetime (time to reach 80% of the peak performance) of 490 hours (*49*). Current state-of-the-art stable perovskite solar cells predominantly adopt a narrower-bandgap perovskite adsorber, that is, $FAPbI_3$ (*4*, *9*, *21*, *23*, *48*, *50*, *51*). However, comparing the stability of mixed-cation, mixed-halide perovskite solar cells with $FAPbI_3$-like perovskites is not straightforward because of inherent differences in degradation pathways (*52*). Nonetheless, our results show a notable advancement in stability when benchmarking against a range of reported compositions. Our mixed-cation, mixed-halide perovskite solar cells rank among the best in terms of operational longevity and demonstrate some of the most promising outcomes reported to date (table S3), especially given the rigorous ISOS-L-3 protocol that we used (*47*), which includes full-spectrum simulated sunlight at an open-circuit condition (*53*). Importantly, only a few studies have used a light source that replicates the full spectrum of sunlight for stability testing (table S3).

After establishing the enhanced operational stability of AEAPTMS-treated cells, as evidenced by their prolonged efficiency retention under the stringent aging conditions discussed above, we further examined their resilience to environmental stressors. One such stressor is water ingression (*54*). As presented in movie S7, soon after we dropped a water droplet onto the $Cs_{13}Br_{10}$ films, we observed a stark contrast between the AEAPTMS-treated and reference perovskite films: The reference immediately turned yellow, indicating rapid hydration and disintegration of perovskite crystalline structures, whereas the AEAPTMS-treated thin perovskite films demonstrated notable resistance, lasting >20 s before showing any signs of partial discoloration.

However, we still observed that, even when using a glass coverslip for encapsulation with epoxy resin edge sealing (as shown in fig. S36, A and B), a capping layer of CYTOP (an amorphous fluoropolymer) to coat the completed devices was required to obtain the best stability results. In the absence of an "on-cell capping layer," cell areas underwent discoloration (fig. S36C). Because the cells were encapsulated in an N_2-filled glove box, we assumed that this discoloration was caused by the loss of iodine during photoinduced degradation, which would leave voids in the film and react with the metallic electrodes (*52*, *55*). However, when comparing the EQE spectra measured from those aged cells (fig. S37), we did not observe a substantial change in the EQE onset energy. This finding suggested that insignificant or negligible compositional change occurred during aging. However, the reference cells suffered from more severe panchromatic deterioration in EQE than the AEAPTMS-treated cells, consistent with the more severe drop in J_{SC}. Notably, the dips in the EQE spectra appeared to result from some intermittent electronic failure of the device, such as sporadic "internal shunting" in the aged devices, which manifested as fluctuating impacts on the EQE at different wavelengths in each measurement (fig. S38).

Given the observed variations in cell performance during aging (Fig. 4, A and B, and fig. S31), we conducted PL imaging of cells to elucidate how the AEAPTMS passivation enhanced long-term stability (*56*). We present the PL-derived QFLS images (see supplementary text) of the representative full-area 0.25-cm^2 AEAPTMS-based and reference cells at different aging stages in Fig. 4, C and D, and fig. S39. Intriguingly, even the reference cell maintained relatively high and stable QFLS maps, comparable to those of its initial state, for up to 300 hours. This stability was evidenced by only 2.8% relative decay in the QFLS median (from 1.16 to 1.13 eV; Fig. 4G), as shown in the corresponding QFLS maps of the reference cells (fig. S39B).

Yet after 600 hours of aging, distinguishable regions of lower and higher QFLS appeared in the maps (Fig. 4D and fig. S39B), indicating that the reference cells degraded heterogeneously on a 100-μm- to millimeter-length scale. The QFLS of the complete device should closely correlate with V_{OC}. However, as we show in Fig. 4G and fig. S32, as the reference perovskite cells aged, the difference between the QFLS and V_{OC} became progressively larger and reached ~380 mV by the end of the aging process. This result indicates that either (i) an energetic shift occurred at one or both charge-selective contacts or (ii) the selectivity for electrons or holes of one of the contacts was reduced. For the reference cell, in addition to loss in V_{OC}, there were also appreciable losses in the other PV performance parameters (figs. S33 and S34).

Therefore, the QFLS images suggest that the perovskite absorber could remain relatively intact when subjected to rigorous 85°C light-soaking aging conditions, whereas other parts of the cell may have undergone severe deterioration. Especially, during aging of the reference devices, substantial decay in all the PV parameters, as exemplified in figs. S32 to S34, with the *J-V* curves shown in fig. S35, suggests a range of detrimental effects, such as poor charge extraction, elevated series resistance, and degraded contact properties. The AEAPTMS-treated cells, on the other hand, exhibited even less deterioration in QFLS and remained homogeneous throughout aging. Specifically, whereas the QFLS median was initially 1.23 eV at 0 hours, this value only dropped to 1.19 eV at 300 hours and to 1.17 eV at 1200 hours (Fig. 4, C and G, and fig. S39A).

The QFLS maps did not appear to directly correlate with the sequence of degradation levels in cells (Fig. 4G). As a result, we turned to an alternative metric—the luminescence-derived "charge collection quality" (Q_{col}; see supplementary text)—which should qualitatively scale with a cell's J_{SC} (*56*). Here, we determined the fraction of the PL, which is quenched at short circuit versus open circuit, and assumed that all of the quenched PL at short circuit resulted from charge extraction. Figure 4, E and F, shows the Q_{col} maps for the fresh and 600-hour aged devices, and in fig. S40, we present our complete dataset of Q_{col} throughout the aging process. Consistent with the macroscopic device *J-V* measurements, the reference cell showed

a substantial reduction in Q_{col} after aging (Fig. 4F). The median dropped from 0.96 in its initial state to 0.42 after aging for 600 hours (see Fig. 4H), indicating a decay of >56%. Notably, the regions of lower Q_{col} mostly correlated with the same regions of lower QFLS. Interestingly, even for the reference cells, quite large regions of high Q_{col} remained after aging for 300 hours (fig. S40B), indicating that the degradation originated from certain defective areas rather than being homogeneous across the entire device (Fig. 4F and fig. S40B). By contrast, the AEAPTMS-treated cells exhibited an even higher initial median Q_{col} (0.99; Fig. 4H), which only dropped to 0.91 (see Fig. 4H) and remained relatively homogeneous after 1200 hours of aging (Fig. 4E and fig. S40A).

We note that although our most stable devices exhibited an approximately linear decay during our stress testing, for both the reference and AEAPTMS-treated devices, we observed that some cells experienced positive light soaking (i.e., performance gain) or burn-in (i.e., early decay) during aging (Fig. 4B and fig. S31B). However, the origin of these differences is not clear and beyond the scope of this study.

Discussion

Our findings demonstrate that amino-silane molecules, with varying primary, secondary, and tertiary amine functional groups, substantially affect the PLQY, crystalline order, and charge-carrier mobility of metal-halide perovskites. In our study, AEAPTMS emerged as an exceptional surface passivator, establishing a strong bonding affinity with the perovskite surface. Notably, the AEAPTMS treatment substantially increases the PLQY of perovskites with bandgaps ranging from 1.6 to 1.8 eV, propelling their radiative performance closer to the theoretical thermodynamic limits. More importantly, AEAPTMS-treated perovskite solar cells exhibit state-of-the-art long-term stability under strenuous elevated temperature light-soaking aging conditions, highlighting the potential of our passivation strategy in advancing highly durable and efficient perovskite PV technologies.

REFERENCES AND NOTES

1. R. E. Brandt *et al*., *Chem. Mater.* **29**, 4667–4674 (2017).
2. Y. Zhou, I. Poli, D. Meggiolaro, F. De Angelis, A. Petrozza, *Nat. Rev. Mater.* **6**, 986–1002 (2021).
3. S. Yu *et al*., *Science* **382**, 1399–1404 (2023).
4. S. M. Park *et al*., *Nature* **624**, 289–294 (2023).
5. N. K. Noel *et al*., *ACS Nano* **8**, 9815–9821 (2014).
6. Q. Jiang *et al*., *Nat. Photonics* **13**, 460–466 (2019).
7. J. Park *et al*., *Nature* **616**, 724–730 (2023).
8. H. Tsai *et al*., *Nature* **536**, 312–316 (2016).
9. S. M. Park *et al*., *Science* **381**, 209–215 (2023).
10. B. Guo *et al*., *Nat. Photonics* **16**, 637–643 (2022).
11. Y. Yuan *et al*., *Nat. Mater.* **23**, 391–397 (2024).
12. R. J. E. Westbrook *et al*., *J. Am. Chem. Soc.* **143**, 12230–12243 (2021).
13. S. You *et al*., *Science* **379**, 288–294 (2023).
14. L. Wu *et al*., *Langmuir* **33**, 12689–12696 (2017).
15. Y. Hassan *et al*., *Nature* **591**, 72–77 (2021).
16. I. L. Braly *et al*., *Nat. Photonics* **12**, 355–361 (2018).
17. Z. Iqbal *et al*., *ACS Energy Lett.* **8**, 4304–4314 (2023).
18. S. Jariwala *et al*., *Chem. Mater.* **33**, 5035–5044 (2021).
19. J. Pothoof, R. J. E. Westbrook, R. Giridharagopal, M. D. Breshears, D. S. Ginger, *J. Phys. Chem. Lett.* **14**, 6092–6098 (2023).
20. Y. Shi *et al*., *ACS Energy Lett.* **7**, 4081–4088 (2022).
21. C. Li *et al*., *Science* **379**, 690–694 (2023).
22. A. J. Ramadan, R. D. J. Oliver, M. B. Johnston, H. J. Snaith, *Nat. Rev. Mater.* **8**, 822–838 (2023).
23. C. Liu *et al*., *Science* **382**, 810–815 (2023).
24. Q. Jiang *et al*., *Nature* **611**, 278–283 (2022).
25. Z. Wang *et al*., *Nature* **618**, 74–79 (2023).
26. Y. H. Lin, H. Faber, S. Rossbauer, T. D. Anthopoulos, *Appl. Phys. Lett.* **102**, 193516 (2013).
27. R. D. J. Oliver *et al*., *Energy Environ. Sci.* **15**, 714–726 (2022).
28. R. Lin *et al*., *Nature* **620**, 994–1000 (2023).
29. S. Zhou *et al*., *Nature* **624**, 69–73 (2023).
30. R. He *et al*., *Nature* **618**, 80–86 (2023).
31. P. K. Nayak, S. Mahesh, H. J. Snaith, D. Cahen, *Nat. Rev. Mater.* **4**, 269–285 (2019).
32. P. Caprioglio *et al*., *Nat. Commun.* **14**, 932 (2023).
33. L. M. Herz, *ACS Energy Lett.* **2**, 1539–1548 (2017).
34. S. Jariwala *et al*., *Joule* **3**, 3048–3060 (2019).
35. L. Zhao *et al*., *Sci. Adv.* **8**, eabo3733 (2022).
36. A. J. Knight *et al*., *ACS Energy Lett.* **6**, 799–808 (2021).
37. S. G. Motti *et al*., *Adv. Funct. Mater.* **30**, 1909904 (2020).
38. N. K. Noel *et al*., *Energy Environ. Sci.* **10**, 145–152 (2017).
39. Z. Zhou *et al*., *Angew. Chem. Int. Ed.* **54**, 9705–9709 (2015).
40. C. Eames *et al*., *Nat. Commun.* **6**, 7497 (2015).
41. J. M. Azpiroz, E. Mosconi, J. Bisquert, F. De Angelis, *Energy Environ. Sci.* **8**, 2118–2127 (2015).
42. D. Ghosh, A. Aziz, J. A. Dawson, A. B. Walker, M. S. Islam, *Chem. Mater.* **31**, 4063–4071 (2019).
43. J. M. Ball, A. Petrozza, *Nat. Energy* **1**, 16149 (2016).
44. M. B. Johnston, L. M. Herz, *Acc. Chem. Res.* **49**, 146–154 (2016).
45. J. Xue, R. Wang, Y. Yang, *Nat. Rev. Mater.* **5**, 809–827 (2020).
46. C. Ma *et al*., *Science* **379**, 173–178 (2023).
47. M. V. Khenkin *et al*., *Nat. Energy* **5**, 35–49 (2020).
48. H. Chen *et al*., *Nat. Photonics* **16**, 352–358 (2022).
49. D. P. McMeekin *et al*., *Nat. Mater.* **22**, 73–83 (2023).
50. M. Wang *et al*., *Nat. Energy* **8**, 1229–1239 (2023).
51. P. Shi *et al*., *Nature* **620**, 323–327 (2023).
52. Y.-H. Lin *et al*., *Science* **369**, 96–102 (2020).
53. K. Domanski, E. A. Alharbi, A. Hagfeldt, M. Grätzel, W. Tress, *Nat. Energy* **3**, 61–67 (2018).
54. S. Yang *et al*., *Science* **365**, 473–478 (2019).
55. F. Fu *et al*., *Energy Environ. Sci.* **12**, 3074–3088 (2019).
56. A. Dasgupta *et al*., *ACS Energy Lett.* **7**, 2311–2322 (2022).

ACKNOWLEDGMENTS

Funding: This work was partially funded by the Engineering and Physical Sciences Research Council (EPSRC), UK (EP/X038777/1). Y.-H.L., X.-L.C., and F.S.Y.Y. acknowledge support from the Early Career Scheme (no. 26210623) from the Hong Kong Research Grant Council. M.S.I. and V. acknowledge the Department of Materials at the University of Oxford and are grateful to the UK's HEC Materials Chemistry Consortium (EP/X035859/1) for the use of the ARCHER2 high-performance computing facilities. R.D.J.O. and A.D. acknowledge the Peierls Scholarship for funding their studentships. Q.Y. acknowledges the support of Rank Prize through a Return to Research grant. XMaS is a UK national research facility supported by the EPSRC. F.Y. is grateful to all the ESRF beamline team staff for their support. M.B.J. thanks the EPSRC for an Established Career Fellowship (EP/T025077/1).

Author contributions: Y.-H.L. and H.J.S. conceived the ideas. H.J.S. supervised the project and progress. Y.-H.L. developed methodologies, fabricated perovskite samples, conducted current-voltage and stability characterizations on perovskite devices, and coordinated collaborations. V. and M.S.I. conducted and analyzed the computer simulations on molecule-surface interactions. A.D. conducted PL imaging measurements. F.Y. conducted XRD and GIWAXS measurements and their analyses. R.D.J.O. conducted PLQY, EQE, and EQE_{EL} measurements and helped with mechanistic analyses. X.-L.C. conducted TOF-SIMS measurements and performed XRD pattern analyses. A.M.U. conducted THz photoconductivity measurements and early x-ray and PL analyses. M.M.M. conducted SEM measurements and helped optimize methodologies. X.S. conducted radiative efficiencies analyses and literature comparison. Q.Y. conducted evaporated ETL optimization. M.G.C. set up solar characterization facilities. F.S.Y.Y., M.B.J., N.K.N., and L.M.H. assisted with characterization analyses and supervised their group members who contributed to this work. Y.-H.L., V., F.Y., X.-L.C., M.S.I., and H.J.S. wrote the first draft of the manuscript. All the authors discussed the results and contributed to the writing of the manuscript. **Competing interests:** H.J.S. is a founder and CSO of Oxford Photovoltaics Ltd. M.G.C. is a director and co-owner of Ark Metrica Ltd. Oxford University has filed patents related to the content of this work. All the other authors declare no competing interests. **Data and materials availability:** All data are available in the main text or the supplementary materials.

SUPPLEMENTARY MATERIALS

science.org/doi/10.1126/science.ado2302
Materials and Methods
Supplementary Text
Figs. S1 to S40
Tables S1 to S3
References (*57–80*)
Movies S1 to S7

Submitted 24 January 2024; accepted 4 April 2024
10.1126/science.ado2302